**Electronic Supplementary Information**

# Effect of electron structure on the catalytic activity of $LaCoO_3$ perovskite towards toluene oxidation

Hanlin Chen [a, b, d, f], Peng Liu [a, b, f], Gaoling Wei [c], Yu Huang [e], Xiaoju Lin [a, b, f], Xiaoliang Liang [a, b, f*], Jianxi Zhu [a, b, f]

[a] CAS Key Laboratory of Mineralogy and Metallogeny/Guangdong Provincial Key Laboratory of Mineral Physics and Materials, Guangzhou Institute of Geochemistry, Chinese Academy of Sciences, Guangzhou 510640, P.R. China;

[b] CAS Center for Excellence in Deep Earth Science, Guangzhou, 510640, China;

[c] National-Regional Joint Engineering Research Center for Soil Pollution Control and Remediation in South China, Guangdong Key Laboratory of Integrated Agro-environmental Pollution Control and Management, Institute of Eco-environmental and Soil Sciences, Guangdong Academy of Sciences, Guangzhou 510650, China;

[d] School of Environmental Science and Technology, Guangdong University of Petrochemical Technology, Maoming 525000, P.R. China;

[e] Key Laboratory of Aerosol Chemistry and Physics, State Key Lab of Loess and Quaternary Geology (SKLLQG), Institute of Earth Environment, Chinese Academy of Sciences, Xi'an 710061, China.

[f] University of Chinese Academy of Sciences, Beijing 100049, P.R. China.

## Experimental section

### Materials and methods

*Catalyst synthesis*

$LaCoO_3$ perovskite was prepared by a one-pot sol-gel method.[1] $La(NO_3)_3 \cdot 6H_2O$, $Co(NO_3)_2 \cdot 6H_2O$, and citric acid (CA) of analytical grade were dissolved in a mixed solvent ($V_{H_2O}$:$V_{ethanol}$ = 2:1) at a mole ratio of $La^{3+}$:$Co^{2+}$:CA equal to 1:1:2 and a $La^{3+}$ concentration of 10 mmol $L^{-1}$. The solution was stirred for 30 min, sonicated for 10 min at room temperature, and dried in a vacuum oven at 90 °C. To obtain crystallized $LaCoO_3$, the precursor was calcined at 500, 600, 700, 800, 900, and 1000 °C for 5 h with a heating rate of 5 °C $min^{-1}$. The obtained solid was ground, sieved to 40-60 mesh, and labeled as LCO-T, where T was the calcination temperature. The sample calcinated at 500 °C shows a low crystalline perovskite phase (Fig. S1).

*Catalyst characterization*

Powder X-ray diffraction (PXRD) patterns were recorded between 20° and 80° ($2\theta$) at a step of 1° $min^{-1}$ on a Bruker D8 advance diffractometer with Cu K$\alpha$ radiation (40 kV and 40 mA). The crystalline size was determined using Scherrer's equation. The transmission electron micrograph (TEM) and electron energy loss spectroscopy (EELS) analyses were performed on a FEI Talos F200S with a spherical aberration corrector. All the particles were dispersed in ethanol on a carbon-coated copper grid. Specific surface area (SSA) measurements were carried out by the BET method based on $N_2$ physisorption capacity at 77 K on a Micromeritics ASAP 2020 instrument.

Fourier transform infrared spectra (FTIR) were recorded on a Bruker Vector 70 spectrometer using KBr as the substrate.

The $H_2$ temperature programmed reduction ($H_2$-TPR) and temperature programmed desorption of oxygen ($O_2$-TPD) were carried out on a Beijing Builder PCA-1200 chemisorption instrument equipped with a TCD detector. All the flow rates were set at 30 mL $min^{-1}$. $H_2$-TPR was evaluated in the range of 30-900 °C at a heating rate of 10 °C $min^{-1}$. The 100.0 mg sample was preheated at 250 °C under Ar for 30 min. $O_2$-TPD was evaluated in the range of 40-800 °C at a heating rate of 10 °C $min^{-1}$ under He flow. 100.0 mg sample was pretreated at 250 °C for 1 h and cooled to 40 °C under $O_2$.

The temperature programmed reduction of toluene (toluene-TPR) and temperature programmed desorption of toluene (toluene-TPD) were performed on a laboratory-made apparatus. For toluene-TPR, 50.0 mg sample after pretreatment by $N_2$ at 150 °C was flowed through by 50 mL $min^{-1}$ of 500 ppm/$N_2$, where the temperature was raised from 30 to 550 °C with a rate of 5 °C $min^{-1}$. For toluene-TPD, 50.0 mg sample was purged under Ar atmosphere at 100 °C for 1 h. After cooling to room temperature, 50 mL $min^{-1}$ of 500 ppm/air was introduced until adsorption saturation. Then, the sample was purged under an $N_2$ flow to remove the weakly absorbed species. Finally, the temperature was increased at a rate of 5 °C $min^{-1}$ from 30 to 550 °C under 50 mL $min^{-1}$ of $N_2$. The $CO_2$ concentration was online monitored by a non-dispersive infrared $CO_2$ analyzer. For LCO-800, LCO-900, and LCO-1000 catalysts, the amount of generated $CO_2$ was below the detection limit. In most cases, the signal of toluene (m/z

= 91 and 92) was too weak to be recognized by a mass spectrometer.

The temperature-dependent magnetization was measured in a SQUID-VSM system at a magnetic field of 500 Oe in the temperature range of 5-300 K under field cooling conditions. Based on the magnetization results, the $e_g$ occupancy of Co cations in LCO-T samples was calculated (Text S1). The core level spectra and valence band (VB) spectra of the samples were investigated by XPS using a Thermo Fisher K-Alpha instrument equipped with an Al Kα source ($h\nu$=1486.6 eV). The pass energy for the full spectrum was 50 eV, while the pass energy for the spectra of a single element and valence band was 30 eV. The charge shift was corrected by adjusting the binding energy of C 1s to 284.8 eV. The O p-band center relative to $E_F$ can be obtained by VB spectra through Gaussian-Lorentzian fitting (Text S2). All the spectra were subtracted with a Shirley-type background.

*Toluene oxidation*

The catalytic oxidation of toluene by LCO-T was performed in a conventional fixed-bed reactor in the temperature range of 100-400 °C under atmospheric pressure. 100.0 mg of catalyst was loaded in a quartz tube reactor (i.d. = 6 mm) supported by a porous quartz plate. Gaseous toluene was generated by flowing $N_2$ into liquid toluene at 0 °C. The inlet gas was composed of 500 ppm toluene and 20 vol% oxygen balanced by $N_2$. The total flow rate was 100 mL $min^{-1}$, corresponding to a gas hourly space velocity (GHSV) of 60 000 $cm^3$ $g^{-1}$ $h^{-1}$. The toluene oxidation efficiency was expressed by the $CO_2$ generation efficiency (Eq. (1)):

$$CO_2 \text{ generation efficiency} = C_{CO_2}/C^*_{CO_2} \times 100\% \quad (1)$$

where $C_{CO_2}$ and $C^*_{CO_2}$ are the $CO_2$ concentrations in the effluent at different temperatures and those when toluene was completely oxidized to $CO_2$, respectively. The concentration of $CO_2$ in the effluent was analyzed online by a non-dispersive infrared $CO_2$ analyzer (Beijing Huayun GXH-3010E).

**Text captions**

**Text S1.** Comparison of the technologies for VOC abatement.

**Text S2.** Results and discussion of EELS spectra.

**Text S3.** Calculation details of $e_g$ occupancy.

**Text S4.** Calculation details of O p band center relative to the $E_{F.}$

**Text S5.** Calculation details of apparent activation energy.

**Text S6.** Comparison of the catalytic activity of reported cobalt-related catalysts towards toluene oxidation.

**Text S7.** Calculation details of specific reaction rate.

**Text S1.** Comparison of the technologies for VOC abatement.

Among the destructive technologies for VOC abatement, thermal incineration and catalytic oxidation are two common routes for the removal of VOCs with medium-high concentration (> 5000 mg $m^{-3}$).[2, 3] Conventional thermal incineration can completely destruct high concentration of VOCs at the temperature as high as 800–1200 °C, while catalytic oxidation is typically operated at lower temperature (200–500 °C or even lower) with less formation of dioxins and noxious products, and is more energy-efficient.[4]

Compared to destruction methods, non-destructive methods including adsorption and condensation have their own advantages and disadvantages.[5] Absorption is widely used as a mature method to effectually remove high concentration of water-soluble VOCs,[6] but usually comes with the challenges for the subsequent treatment of spent solvent and high cost for maintenance. Condensation can recover VOCs in quantity through transforming them into liquid at lower temperature or higher pressure.[7] Nonetheless, due to the high processing cost, condensation usually deals with the valuable VOCs at high concentration,[8] and is limited by the disposal of spent coolant during the condensation process.[9]

**Text S2.** Results and discussion of EELS spectra.

According to the XPS analysis, the valence of surface Co is +3. To investigate the valence of Co in the bulk of LCO-T, the electron energy loss spectroscopy (EELS) was performed under STEM condition. Figs. 1d and S6 shows the EELS spectra at Co L-edges from the center to the edge of LCO-T nanoparticle, which is sensitive to the electronic structure from the bulk and the surface. The EELS spectra display two peaks at ca. 780.4 and 795.4 eV, attributed to the $L_3$ and $L_2$ peaks in Co L-edges, respectively. For Co $L_{2,3}$-edges which originate from the excitations from the inner 2p to unoccupied 3d orbitals, the energy onset of $L_3$ peak and the white-line intensity ratio ($I_3/I_2$, where the $I_2$ and $I_3$ are the integrated intensity of $L_2$ and $L_3$ peaks) are sensitive to the oxidation state. Co $L_{2,3}$-edges taken from the surface region are similar to those from the center region, including peak intensities and energies. And no noticeable change in the $I_3/I_2$ ratio between the bulk and surface is found. Thus, the oxidation state of Co is +3 in LCO-T (Lines 103-117).[10-13]

**Text S3.** Calculation details of $e_g$ occupancy.

Based on the magnetization curves, the temperature-dependent susceptibility ($\chi$) was calculated by Eq. (2).

$$\chi = M/\mathrm{H} \quad (2)$$

where M is the temperature-dependent magnetization (Fig. S5.a) and H is the magnetic field strength, i.e., 500 Oe. Based on the Curie-Weiss law (Eq. (3)), the Curie constant ($C$) of LCO-T samples can be obtained from the slope of the straight lines above the paramagnetic transition temperatures ($\Theta$) by plotting $\chi^{-1}$ as a function of temperature $T$ through regression (Fig. S5b, Table 2).

$$\chi^{-1} = (T-\Theta)/C \quad (3)$$

According to Langevin theory, the Curie constant ($C$) is correlated with the Boltzmann constant ($k_B$, $1.38\times10^{-23}$ J/K), Avogadro number ($N_A$, $6.02\times10^{23}$/mol), Bohr magneton ($\mu_B$, $9.27\times10^{-24}$ J/T), Lande factor (g) and total angular momentum quantum number ($J$) (Eq. (4)). As $k_B$, $N_A$, and $\mu_B$ are constant, Eq. (4) can be changed to Eq. (5).

$$C = N_A g^2 \mu_B^2 J(J+1)/3k_B \quad (4)$$

$$8C = g^2 J(J+1) \quad (5)$$

Combined with the Quantum theory (Eq. (6)), Eq. (5) can be changed to Eq. (7). The effective magnetic moments ($\mu_{eff}$ with $\mu_B$ as a unit) can be calculated and are shown in Table 2.

$$\mu_{eff}^2 = g^2 J(J+1)\mu_B^2 \quad (6)$$

$$\mu_{eff}^2 = 8C\mu_B^2 \quad (7)$$

160 Based on the theory of paramagnetism (Eq. (8)), the volume fractions of metals in
161 HS and LS states can be calculated (Table S2), from which the $e_g$ value can be
162 obtained (Eqs. (9)-(10), Table 2) .[14, 15]

163 $$\mu_{eff}=g\mu_B(S_{HS}(S_{HS}+1)V_{HS}+ S_{LS}(S_{LS}+1)V_{LS})^{1/2} \quad (8)$$

164 $$V_{HS} + V_{LS} = 1 \quad (9)$$

165 $$x = 2V_{HS} \quad (10)$$

166 where $S_{HS}$ and $S_{LS}$ are $S$ values equal to 2 and 0, respectively, and $V_{HS}$ and $V_{LS}$ are
167 the volume fractions in HS and LS states, respectively.
168

**Text S4.** Calculation details of O p band center relative to the $E_{F.}$

VB spectra were fitted by Gaussian-Lorentzian and corrected by background using the Shirley approach. After background subtraction, the asymmetrical VB spectra of LCO-T were deconvoluted into four symmetrical peaks of A, B, C, and D (Fig. 4). The peaks A, C, and D are attributed to the Co 3d state, while the peak B is mainly attributed to the O 2p state.[15] The O p-band center relative to the $E_F$ can be calculated by Eq. (11).[16, 17]

$$O\ p-band\ center = \frac{\int_{-\infty}^{\infty} x\rho(x)dx}{\int_{-\infty}^{\infty} \rho(x)dx} \quad (11)$$

where $x$ and $\rho(x)$ are the energy and density of electron, respectively.

**Text S5.** Calculation details of apparent activation energy.

The reaction rate ($r_s$, μmol $g^{-1}$ $s^{-1}$) was defined as the number of toluene molecules oxidized over the catalyst per gram per second (Eq. (12)).

$$r_s = (C_{toluene} \times X_{toluene} \times V_{gas})/m \quad (12)$$

where $m$ is the catalyst mass (g), $C_{toluene}$ is the concentration of toluene in the gas mixture (μmol $mL^{-1}$), $X_{toluene}$ is the conversion of toluene (%), and $V_{gas}$ is the total flow rate (mL $s^{-1}$).

The apparent activation energy ($E_a$, kJ $mol^{-1}$) was evaluated by the Arrhenius equation (Eq. (13)) [18].

$$r_s = A \exp(-E_a/RT) \quad (13)$$

where $r_s$ is the reaction rate of toluene (μmol $g^{-1}$ $s^{-1}$), A is the pre-exponential factor, R is the molar gas constant, 8.314 J $mol^{-1}$ $K^{-1}$.

**Text S6.** Comparison of the catalytic activity of reported cobalt-related catalysts towards toluene oxidation.

A comparison on catalytic activity of the as-obtained typical sample has been made with those of the related catalysts reported in the literatures. Under identical reaction condition, LCO-700 is compared to the previously reported cobalt-related catalysts in toluene oxidation. LCO-700 exhibits better catalytic activity (T90 = 220 $^{o}$C) than both spinel-type oxides (e.g., $Co_3O_4$ (T90 = 266 $^{o}$C),[19] CoMnO (T90 = 311 $^{o}$C) [20] and CoAlO (T90 = 319 $^{o}$C),[21]) and perovskite-type oxides (e.g., $La_{0.6}Sr_{0.4}Co_{0.9}Fe_{0.1}O_3$ (T90 = 239 $^{o}$C),[22] $LaCoO_3$/SBA-15 (T90 = 310 $^{o}$C) [23] and $Co_3O_4$/3DOM $La_{0.6}Sr_{0.4}CoO_3$ (T90 = 227 $^{o}$C)).[24]

**Text S7.** Calculation details of specific reaction rate.

The specific reaction rate ($R_s$, μmol $s^{-1}$ $m^{-2}$) of LCO-T catalysts was defined as the number of toluene molecules oxidized over the catalyst per second per square meter (Eq. (14)).

$$R_s = C_{toluene} \times X_{toluene} \times V_{gas} / (S \times m) \quad (14)$$

where $m$ is the catalyst mass (g), $C_{toluene}$ is the concentration of toluene in the gas mixture (μmol $mL^{-1}$), $X_{toluene}$ is the conversion of toluene (%) over LCO-T at 200 °C, $V_{gas}$ is the total flow rate (mL $s^{-1}$) and $S$ is the specific surface area ($m^2$ $g^{-1}$).

**Table captions**

**Table S1.** Lattice parameters, crystal size, particle size and specific surface area (SSA) of LCO-T samples.

**Table S2.** Effective magnetic moment ($\mu_{eff}$) and $e_g$ orbital occupation for different spin states of $Co^{3+}$ ions in LCO-T samples.

**Table S3.** Temperatures for 50% and 90% toluene conversion, apparent activation energies ($E_a$) and SSA-normalized reaction rate over LCO-T catalysts.

**Table S1.** Lattice parameters, crystal size, particle size and specific surface area (SSA) of LCO-T samples.

| Samples | $a_0=b_0$/Å | $c_0$/Å | $V$/Å$^3$ | crystallite size/nm | particle size/nm | SSA/m$^2$ g$^{-1}$ |
|---|---|---|---|---|---|---|
| LCO-600 | 5.423 | 13.146 | 334.76 | 21 | 29 | 10.4 |
| LCO-700 | 5.435 | 13.114 | 335.50 | 21 | 24 | 7.5 |
| LCO-800 | 5.438 | 13.121 | 336.08 | 23 | 34 | 3.8 |
| LCO-900 | 5.424 | 13.206 | 336.42 | 35 | 52 | 1.6 |
| LCO-1000 | 5.423 | 13.211 | 336.53 | 81 | 512 | 1.4 |

223 **Table S2.** Effective magnetic moment ($\mu_{eff}$) and $e_g$ orbital occupation for different

224 spin states of $Co^{3+}$ ions in LCO-T samples.

| Samples | *C*/ emu·K.mol$^{-1}$ | $\mu_{eff}$/ $\mu_B$ | high spin state percentage | low spin state percentage | $e_g$ |
|---|---|---|---|---|---|
| LCO-600 | 1.46 | 3.42 | 46% | 54% | 0.92 |
| LCO-700 | 1.51 | 3.48 | 50% | 50% | 1.00 |
| LCO-800 | 1.98 | 3.98 | 66% | 34% | 1.32 |
| LCO-900 | 2.18 | 4.18 | 73% | 27% | 1.46 |
| LCO-1000 | 2.83 | 4.76 | 94% | 6% | 1.89 |

**Table S3.** Temperatures for 50% and 90% toluene conversion, apparent activation energies ($E_a$) and SSA-normalized reaction rate over LCO-T catalysts.

| Sample | Toluene oxidation activity | | $E_a$/ | SSA-normalized reaction rate |
|---|---|---|---|---|
| | $T_{50}$/°C | $T_{90}$/°C | kJ mol$^{-1}$ | ($R_s$)/μmol s$^{-1}$ m$^{-2}$ |
| LCO-600 | 213 | 223 | 50 | 0.358 |
| LCO-700 | 211 | 220 | 49 | 0.404 |
| LCO-800 | 216 | 240 | 55 | 0.345 |
| LCO-900 | 223 | 250 | 61 | 0.309 |
| LCO-1000 | 259 | 335 | 73 | 0.236 |

**Figure captions**

**Fig. S1** XRD patterns for LCO-T catalysts and the standard card (JCPDS: 25-1060) of hexagonal $LaCoO_3$ perovskite.

**Fig. S2** XRD pattern for LCO-500 sample and the standard card (JCPDS: 25-1060) of hexagonal $LaCoO_3$ perovskite.

**Fig. S3** Element mapping (a), and EDS spectra images (b) of LCO-700, and TEM images and size distribution of LCO-600 (c), LCO-800 (d), LCO -900 (e), and LCO-1000 (f).

**Fig. S4** Survey XPS spectra of LCO-T samples.

**Fig. S5** Co 2p XPS spectra of LCO-T samples.

**Fig. S6** EELS spectra of Co L-edges of LCO-600 (a), LCO-800 (b), LCO-900 (c), and LCO-1000 (d).

**Fig. S7** EELS spectra of La M-edges of LCO-700.

**Fig. S8** Temperature dependent magnetization (a) and temperature dependent of susceptibilities (b) under H = 500 Oe for LCO-T samples.

**Fig. S9** Catalytic stability of LCO-700 at 250 °C. Reaction conditions: [toluene] = 500 ppm, $[O_2]$ = 20%, catalyst mass = 100 mg, total flow rate = 100 mL $min^{-1}$, and GHSV = 60000 $cm^3$ $g^{-1}$ $h^{-1}$.

**Fig. S10** O 2p XPS spectra of LCO-T catalysts.

**Fig. S11** $O_2$-TPD profiles of LCO-T catalysts (a), toluene-TPD profiles of LCO-600 and LCO-700 (b), and $H_2$-TPR (c) and toluene-TPSR profiles (d) of LCO-T catalysts.

**Fig. S12** Relationship between $e_g$ filling and O p-band center relative to the $E_F$ of

LCO-T catalysts.

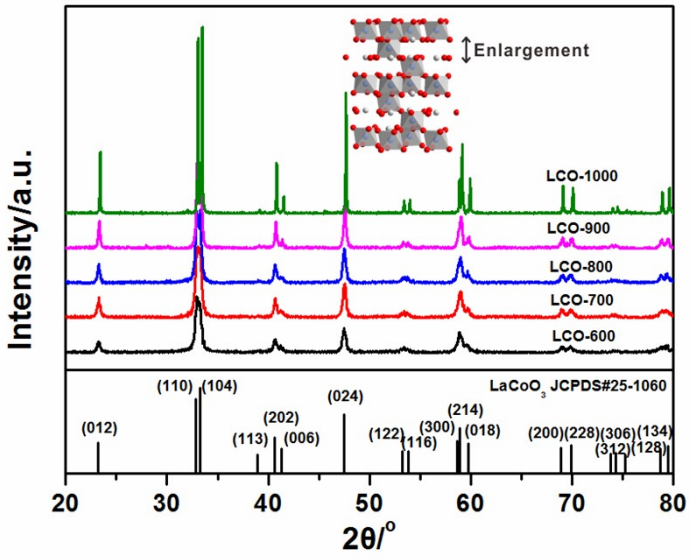


**Fig. S1** XRD patterns for LCO-T catalysts and the standard card (JCPDS: 25-1060) of hexagonal $LaCoO_3$ perovskite.

The XRD patterns of LCO-T well correspond to the standard card of hexagonal $LaCoO_3$ (JCPDS: 25-1060), with diffractions of (012), (110), (104), (202), (006), (024), (122), (116), (300), (214), (018), (200), and (228) planes at $2\theta$ of 23.2°, 33.0°, 33.4°, 40.7°, 41.4°, 47.6°, 53.2°, 53.8°, 59.0°, 59.9°, 69.2°, and 70.2°, respectively (Fig. S1).[25] Apart from perovskite-type $LaCoO_3$, calcinations at 600-1000 °C do not yield any other phases, e.g., $Co_3O_4$ and $La_2O_3$. However, calcinations at higher temperature inevitably improves the crystallinity, as the diffraction patterns become more intense. The crystallite size increases from 21 nm (LCO-600) to 512 nm (LCO-1000). In terms of lattice parameter, the $a_0$ and $b_0$ vary slightly with the calcination temperature, but the $c_0$ increases significantly at higher calcination temperature. This suggests the expansion of unit cell of $LaCoO_3$.

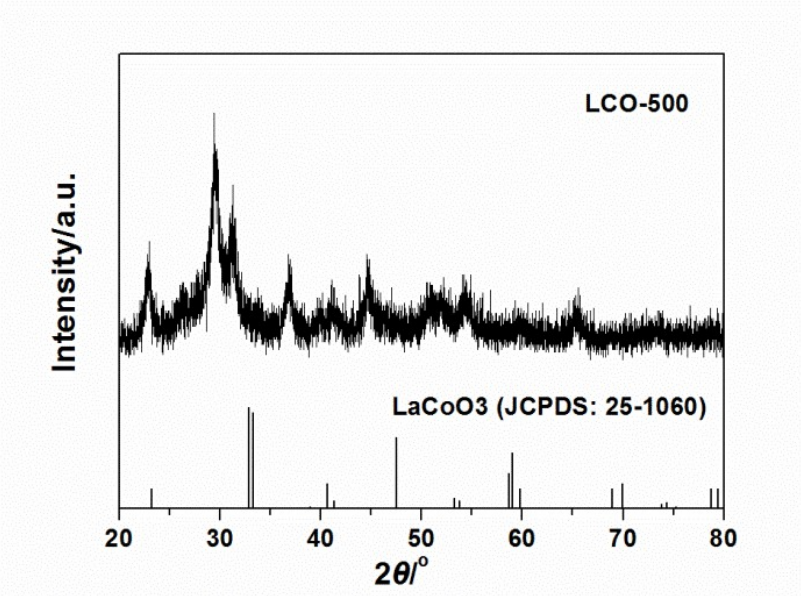


**Fig. S2** XRD pattern for LCO-500 sample and the standard card (JCPDS: 25-1060) of hexagonal $LaCoO_3$ perovskite.

The sample calcinated at 500 °C shows a perovskite phase with low-crystalline (Fig. S2). Furthermore, apart from $LaCoO_3$ perovskite, impure phases, e.g. $Co_3O_4$ and $La_2O_3$ appear.

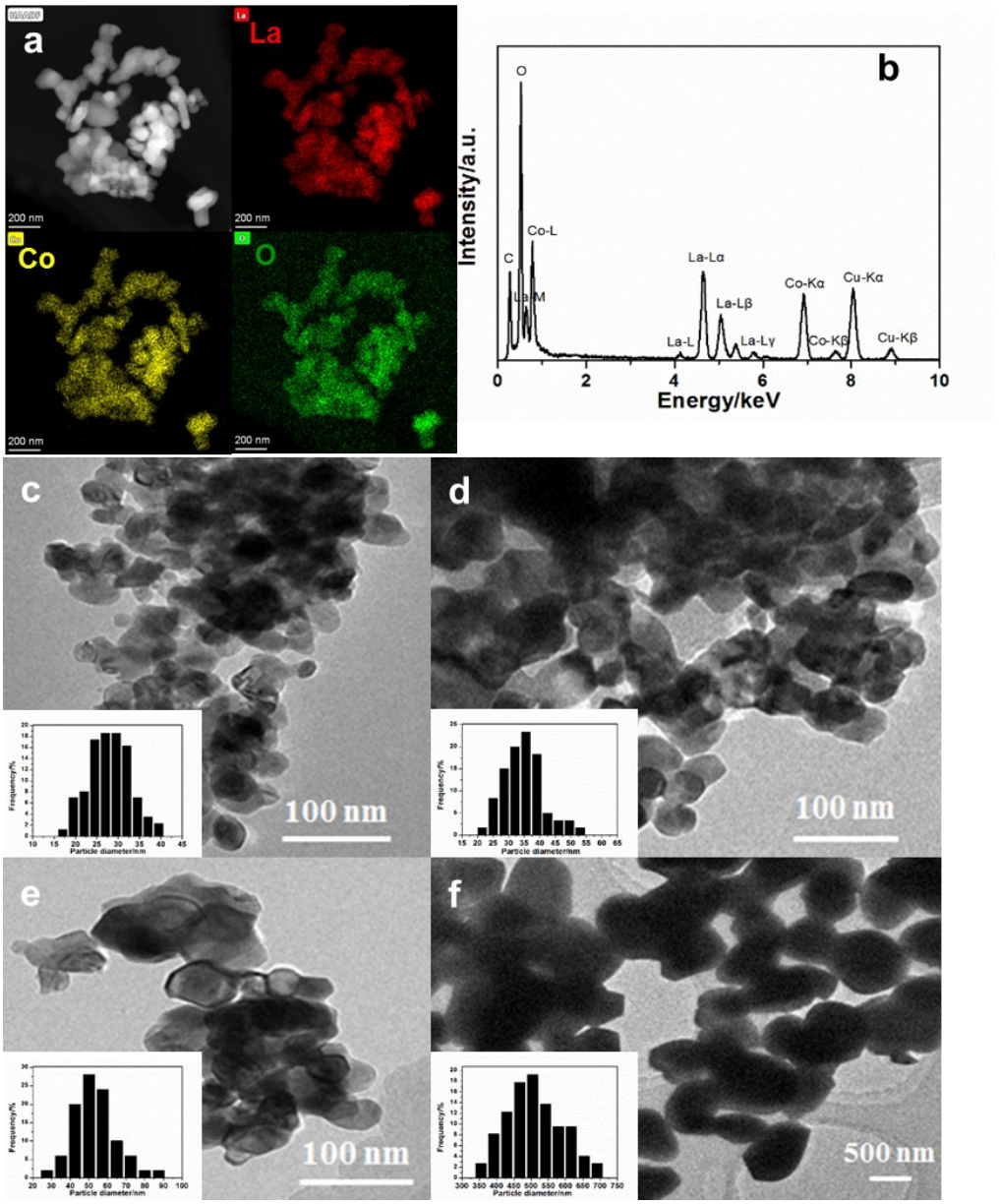


**Fig. S3** Element mapping (a), and EDS spectrum image (b) of LCO-700, and TEM images and size distribution of LCO-600 (c), LCO-800 (d), LCO -900 (e), and LCO-1000 (f).

The EDS mapping indicates the uniform dispersion of La, Co, and O in LCO-700, with a La:Co atomic ratio of 1 (Fig. S3a-b). TEM images display that all the LCO-T samples exhibit many spherical particles interwoven together (Fig. S3c-f). The particle sizes of LCO-600, LCO-800, LCO-900, and LCO-1000 are 29, 34, 52, and 511 nm, respectively.

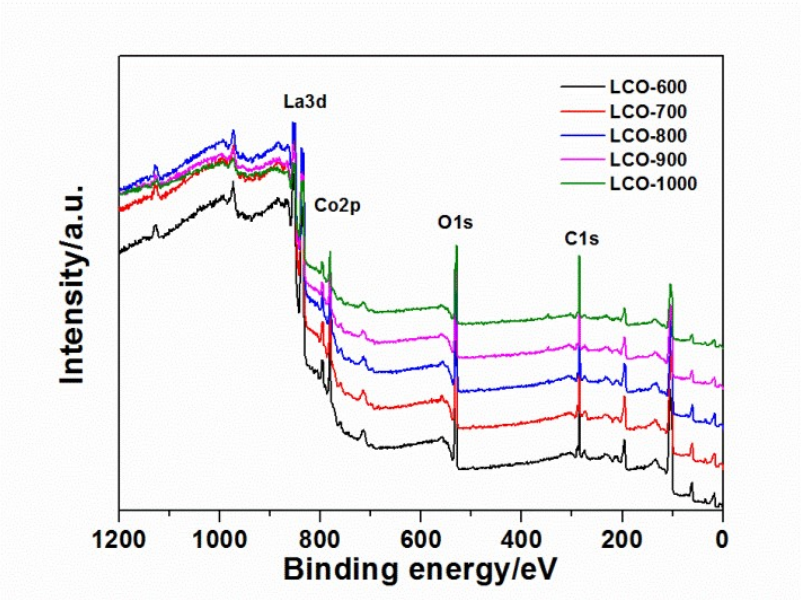


283

284 **Fig. S4** Survey XPS spectra of LCO-T samples.

285 The XPS full-range spectra of LCO-T reveal the presence of La (10.42 at. %), Co
286 (10.32 at. %), and O (79.28 at. %) on the surface (Fig. S4). The La:Co atomic ratio is
287 1, which is in accord with the EDS mapping analysis results. This indicates the same
288 surface chemical composition in LCO-T.

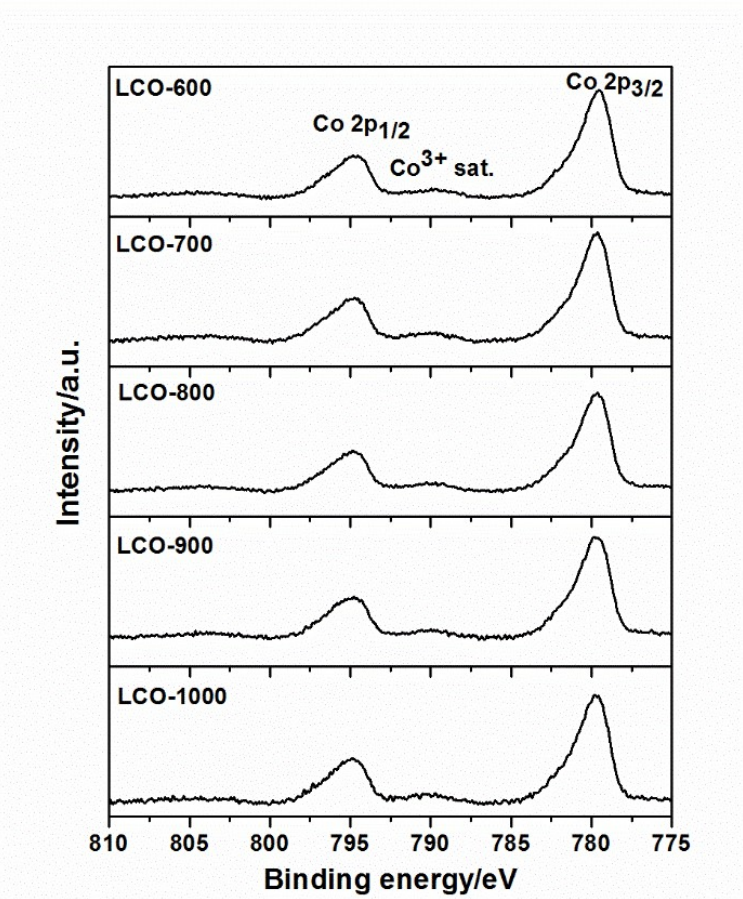


**Fig. S5** Co 2p XPS spectra of LCO-T samples.

The Co 2p spectra are composed of Co 2p3/2, Co 2p1/2, and satellite peaks at 779.8, 795.0, and 790.0 eV, respectively (Fig. S5). The binding energy of Co 2p3/2 reveals that the valence of surface Co is +3. [26, 27] The XPS results illustrate that all the LCO-T catalysts have the same Co valence on the surface.

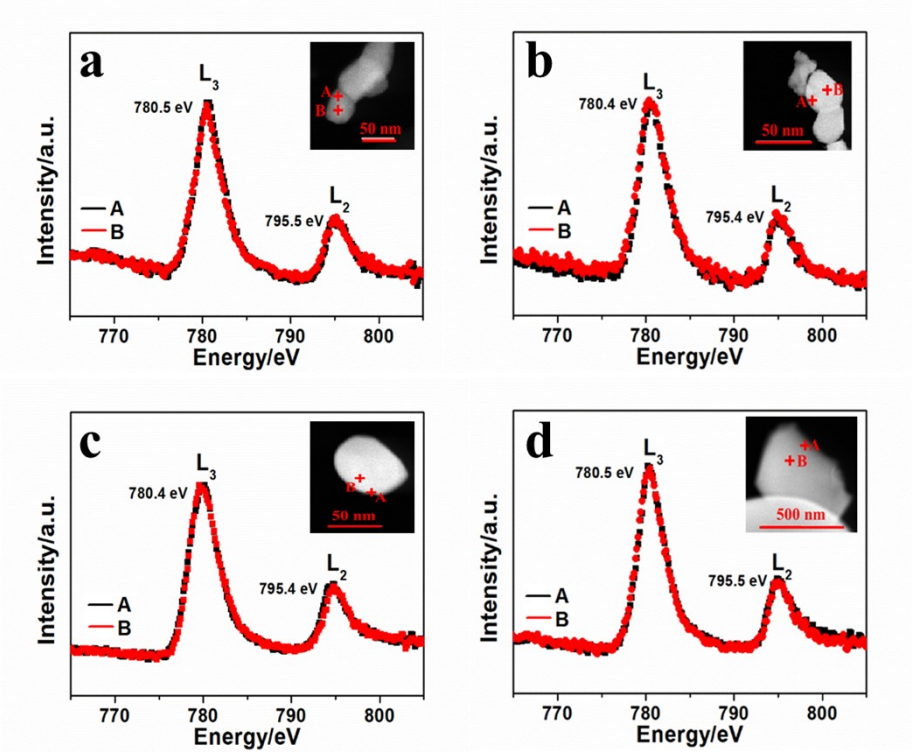


**Fig. S6** EELS spectra of Co L-edges of LCO-600 (a), LCO-800 (b), LCO-900 (c), and LCO-1000 (d).

For all the LCO-T samples, Co $L_{2,3}$-edges taken from the surface region are similar to those from the bulk region, including peak intensities and energy positions. Moreover, no noticeable change in the $I_3/I_2$ ratio between the bulk and surface is found (Fig. S6). Thus, the oxidation state of Co is +3 in LCO-T (Lines 103-111). [12-14]

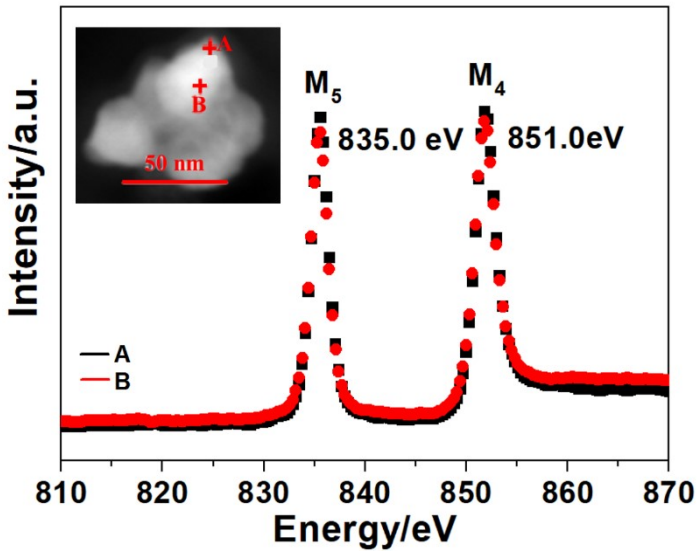


305

306 **Fig. S7** EELS spectra of La M-edges of LCO-700.

307 The valence of La in LCO-T is also investigated by EELS spectra. Fig. R2 shows
308 the EELS spectra at La M-edges from the bulk to the edge of LCO-700 nanoparticle.
309 The EELS spectra display two peaks at ca. 835.0 and 851.0 eV, corresponding to the
310 3d to 4f transitions of the $M_5$ and $M_4$-edges.[28] La $M_{4,5}$-edges taken from the surface
311 region are similar to those from the center region, including peak intensities and
312 energy positions. The EELS spectra of La $M_{4,5}$-edges also prove that La is +3 in LCO-
313 T (Fig. S7).[29-31]

314

315

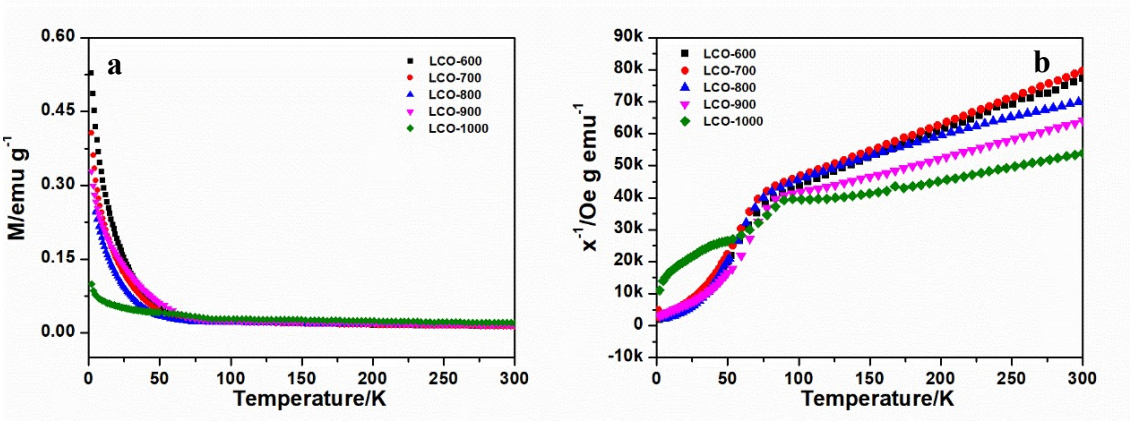


316 **Fig. S8** Temperature dependent magnetization (a) and temperature dependent of susceptibilities (b)
317 under H = 500 Oe for LCO-T samples.

318 The composition of spin states can be indexed by $e_g$ orbital filling. The number of
319 $e_g$ orbital fillings increases with the HS proportion. In Fig. S8, the effective magnetic
320 moment $\mu_{eff}$ can be calculated by $\mu_{eff} = (8C)^{1/2}\mu_B$ (Text S2). For LCO-700, the
321 calculated $\mu_{eff}$ of 3.48 $\mu_B$ is consistent with the values reported for $LaCoO_3$,
322 corresponding to the $Co^{3+}$ ions of half HS and half LS states.[32, 33] The calculated $\mu_{eff}$
323 values of LCO-600, LCO-800, LCO-900, and LCO-1000 are 3.42, 3.98, 4.18, and
324 4.76 $\mu_B$, respectively. The increase in $\mu_{eff}$ with calcination temperature is a distinctive
325 feature of cobaltite, owing to the strong interdependence between Co-Co interactions
326 and the Co spin state.[33] The $e_g$ values of LCO-600, LCO-700, LCO-800, LCO-900,
327 and LCO-1000 are 0.92, 1.00, 1.32, 1.46, and 1.89, respectively (Table 2).
328 Consequently, the unit cell expansion of LCO-T (from 334.76 to 336.53 $Å^3$) can be
329 explained by the increasing population of HS states, ascribed to the larger radii of
330 $Co^{3+}$ with HS (0.610 Å) than that of $Co^{3+}$ with LS (0.545 Å).[34]

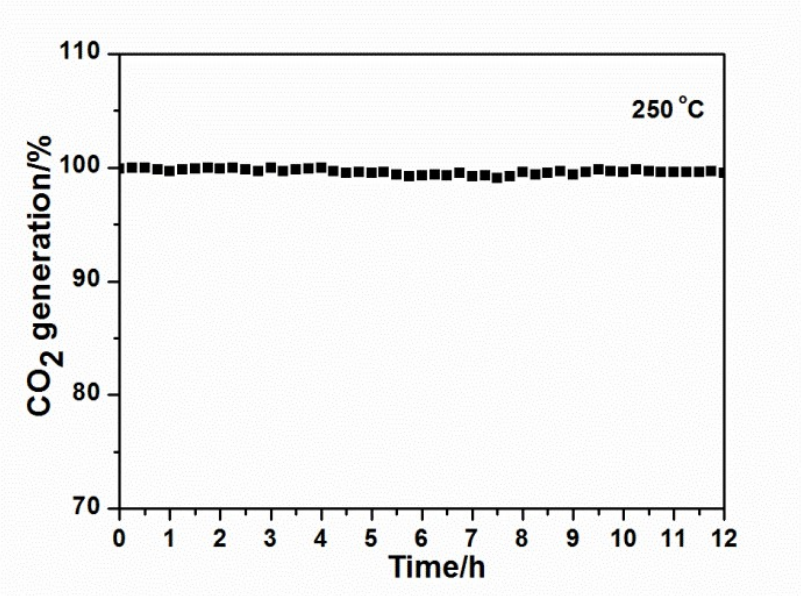


331

332 **Fig. S9** Catalytic stability of LCO-700 at 250 °C. Reaction conditions: [toluene] = 500 ppm, [$O_2$]

333 = 20%, catalyst mass = 100 mg, total flow rate = 100 mL $min^{-1}$, and GHSV = 60000 $cm^3$ $g^{-1}$ $h^{-1}$.

334 LCO-700 shows high stability in the catalytic oxidation of toluene at 250 °C for 12

335 h (Fig. S9).

336

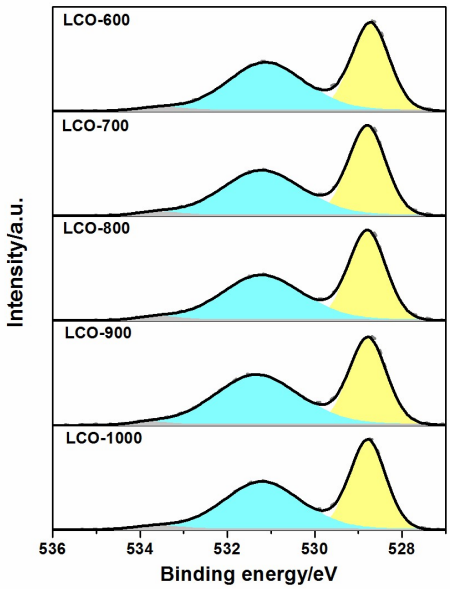


**Fig. S10** O 2p XPS spectra of LCO-T catalysts.

Oxygen species are vital in the VOC oxidation over transition metal oxides.[1] The O 1s XPS spectra of LCO-T display a two-band curve (Fig. S10). The spectra are deconvoluted into three contributions at 528.6, 531.1, and 533.1 eV, attributed to lattice oxygen ($O_{lat}$), surface adsorbed oxygen ($O_{ads}$), and adsorbed water, respectively. The electrophilic $O_{ads}$ including $O^{2-}$, $O_2^{2-}$ or $O^-$,[35] can attack organic molecules in the region of high electron density, leading to the destruction and deep oxidation of the carbon skeleton. Thus, the electrophilic oxygen species on the surface of LCO-T catalysts are responsible for the total oxidation of toluene.[25] For LCO-T, the $O_{ads}/O_{lat}$ ratio decreases in the following order: LCO-700 (1.41) > LCO-600 (1.38) > LCO-800 (1.30) > LCO-900 (1.24) > LCO-1000 (1.17). The $O_{ads}/O_{lat}$ ratio displays a good positive relationship with the SSA-normalized reaction rate $R_s$ ($R^2$ = 0.97) (Fig. 4a). This consolidates the vital role of surface oxygen in the catalytic oxidation of toluene over LCO-T catalysts.

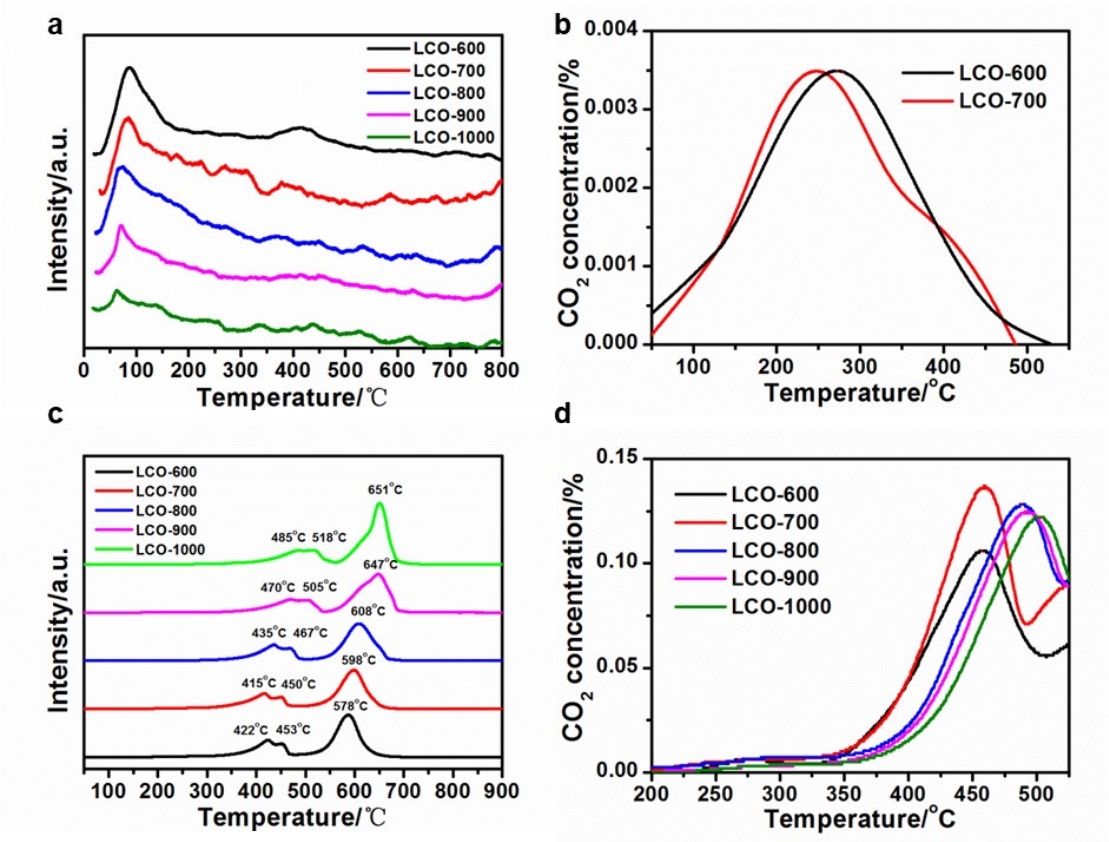


**Fig. S11** $O_2$-TPD profiles of LCO-T catalysts (a), toluene-TPD profiles of LCO-600 and LCO-700 (b), and $H_2$-TPR (c) and toluene-TPSR profiles (d) of LCO-T catalysts.

The mobility of surface oxygen affects the formation of oxygen vacancies and the refilling by gaseous oxygen, which greatly determines the catalytic activity.[36] The composition of oxygen species is investigated by $O_2$-TPD (Fig. S11a). The peaks below 250 °C are attributed to the desorption of adsorbed oxygen ($O_\alpha$), including $O_2$, $O_2^-$, $O_2^{2-}$ or $O^-$, while those in the range of 300-500 °C are attributed to the desorption of labile lattice oxygen ($O_\beta$).[25] The desorption amount of $O_\alpha$ from LCO-T increases as follows: LCO-1000 (1.2 μmol $g^{-1}$) < LCO-900 (9.9 μmol $g^{-1}$) < LCO-800 (21.7 μmol $g^{-1}$) < LCO-600 (24.6 μmol $g^{-1}$) < LCO-700 (26.3 μmol $g^{-1}$).

The $CO_2$ evolved in toluene-TPD is monitored. The LCO-700 evolves similar amount of $CO_2$ to LCO-600, while the peak temperatures for LCO-600 and LCO-700

365 are 274 and 246 °C, respectively, close to the T90 (220-223 °C) in toluene oxidation
366 (Fig. S11b). For LCO-800, LCO-900, and LCO-1000 catalysts, the amount of
367 generated $CO_2$ was below the detection limit. As the temperature of $O_\alpha$ desorption
368 overlaps with that of toluene oxidation, $O_\alpha$ is one of main oxygen species responsible
369 for toluene oxidation.

370 The $H_2$-TPR profiles of $LaCoO_3$ show two main peaks, which are originated from
371 the reduction of $Co^{3+}$ to $Co^{2+}$ and $Co^{2+}$ to $Co^0$, respectively (Fig. S11c). In the low
372 temperature region from 300 to 550 °C, $Co^{3+}$ is reduced to $Co^{2+}$. The second reduction
373 peak from 550 to 650 °C is assigned to the reduction of $Co^{2+}$ to $Co^0$. The reduction of
374 $Co^{3+}$ to $Co^{2+}$ is involved in the oxidation of toluene rather than the reduction of $Co^{2+}$
375 to $Co^0$. Thus, this study focused on the variation in the reduction peak at low-
376 temperature region. The peak temperature of first reduction increases in the following
377 order: LCO-700 (415 °C) < LCO-600 (422 °C) < LCO-800 (435 °C) < LCO-900 (470
378 °C) < LCO-1000 (485 °C). This is consistent with the order of the catalytic activity.

379 The toluene-TPR is performed to reveal the reaction between toluene and lattice
380 oxygen (Fig. S11d). The first reduction peak is assigned to the reduction of $Co^{3+}$ to
381 $Co^{2+}$ by toluene, and the peak temperature for LCO-600, LCO-700, LCO-800, LCO-
382 900, and LCO-1000 is 460, 456, 487, 493, and 505 °C, respectively. The $H_2$-TPR and
383 toluene-TPR results indicate that the $O_\beta$ is also involved in the oxidation of toluene,
384 and the activity of $O_\beta$ decreases as follows: LCO-700 > LCO-600 > LCO-800 > LCO-
385 900 > LCO-1000.

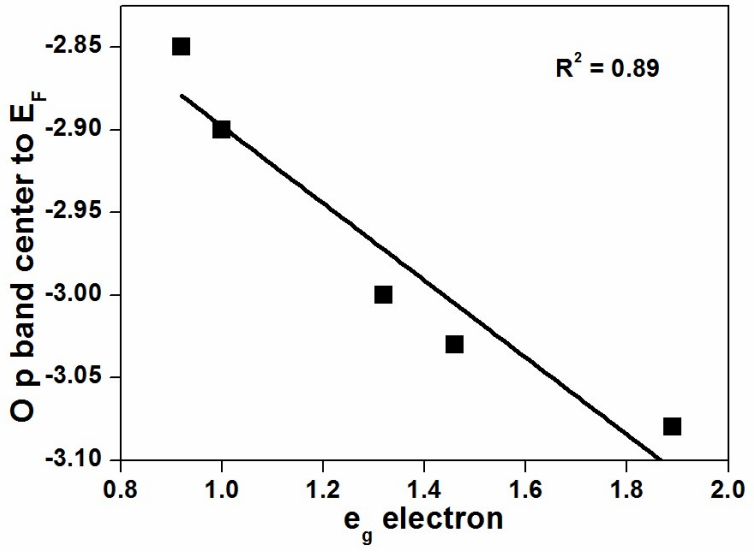


386

387 **Fig. S12** Relationship between $e_g$ filling and O p-band center relative to the $E_F$ of LCO-T catalysts.

388 The relationship between $e_g$ filling and the O p-band center relative to the $E_F$ shows
389 a good linear relationship ($R^2$ = 0.89, Fig. S12). Because the $e_g$ filling determines the
390 oxygen adsorption strength on Co sites, it affects the oxygen adsorption and
391 desorption.[37] These processes are also constrained by the O p-band center relative to
392 the $E_F$. Specifically, for LCO-600, oxygen desorption would be suppressed, because
393 the O p-band center is too close to $E_F$. By contrast, for LCO-1000, the O p-band
394 center is too far from the $E_F$; thus, the oxygen adsorption is difficult, inhibiting the
395 surface oxygen refilling.

396

## References


1. N. A. Merino, B. P. Barbero, P. Ruiz and L. E. Cadus, *J. Catal.*, 2006, **240**, 245-257.
2. C. T. Yang, G. Miao, Y. H. Pi, Q. B. Xia, J. L. Wu, Z. Li and J. Xiao, *Chem. Eng. J.*, 2019, **370**, 1128-1153.
3. K. Everaert and J. Baeyens, *J. Hazard. Mater.*, 2004, **109**, 113-139.
4. Z. X. Zhang, J. Zheng and W. F. Shangguan, *Catal. Today*, 2016, **264**, 270-278.
5. Youn-Suk Son, *Chem. Eng. J.*, 2017, **316**, 609-622.
6. F. Heymes, P. Manno-Demoustier, F. Charbit, J. L. Fanlo and P. Moulin, *Chem. Eng. J.*, 2006, **115**, 225-231.
7. F. I. Khan and A. K. Ghoshal, *J. Loss Prevent. Proc. Indust.*, 2000, **13**, 527-545.
8. P. Dwivedi, V. Gaur, A. Sharma and N. Verma, *Sep. Purif. Technol.*, 2004, **39**, 23-37.
9. M. S. Kamal, S. A. Razzak and M. M. Hossain, *Atmos. Environ.*, 2016, **140**, 117-134.
10. R. F. Klie, J. C. Zheng, Y. Zhu, M. Varela, J. Wu and C. Leighton, *Phys. Rev. Lett.*, 2007, **99**, 47203-47203.
11. J. Gazquez, W. Luo, M. P. Oxley, M. Prange, M. A. Torija, M. Sharma, C. Leighton, S. T. Pantelides, S. J. Pennycook and M. Varela, *Nano Lett.*, 2011, **11**, 973-976.
12. J. H. Kwon, W. S. Choi, Y. K. Kwon, R. Jung, J. M. Zuo, H. N. Lee and M. Kim, *Chem. Mater.*, 2014, **26**, 2496-2501.
13. B. H. Han, D. N. Qian, M. Risch, H. L. Chen, M. F. Chi, Y. S. Meng and Y. Shao-Horn, *J. Phys. Chem. Lett.*, 2015, **6**, 1357-1362.
14. S. M. Zhou, X. B. Miao, X. Zhao, C. Ma, Y. H. Qiu, Z. P. Hu, J. Y. Zhao, L. Shi and J. Zeng, *Nat. Commun.*, 2016, **7**, 11510.
15. Y. Z. Jin, Z. Li, J. Q. Wang, R. Li, Z. Q. Li, H. Liu, J. Mao, C. K. Dong, J.

Yang, S. Z. Qiao and X. W. Du, *Adv. Energy Mater.*, 2018, **8**, 1703469.

16. J. N. Nørskov, F. Studt, F. Abildpedersen and T. Bligaard, *Fundamental Concepts in Heterogeneous Catalysis*, John Wiley and Sons, Inc, 2014.

17. T. Wang, C. Zhang, J. Y. Wang, H. Y. Li and Z. J. Xu, *J. Catal.*, 2020, **390**, 1-11.

18. M. Alifanti, M. Florea, S. Somacescu and V. I. Parvulescu, *Appl. Catal. B-Environ.*, 2005, **60**, 33-39.

19. Y. X. Liu, H. X. Dai, J. G. Deng, L. Zhang and G. S. Guo, *Inorg. Chem.*, 2013, **52**, 8665-8676.

20. D. A. Aguilera, A. Perez, R. Molina and S. Moreno, *Appl. Catal. B-Environ.*, 2011, **104**, 144-150.

21. S. Zhao, K. Z. Li and J. H. Li, *Appl. Catal. B-Environ.*, 2016, **181**, 236-248.

22. J. G. Deng, H. X. Dai, H. Y. Hang, L. Zhang, G. Z. Wang, H. E. Hong and C. T. Au, *Environ. Sci. Technol.*, 2010, **44**, 2618-2623.

23. J. G. Deng, L. Zhang, H. X. Dai and C. T. Au, *Appl. Catal. A-Gen.*, 2009, **352**, 43-49.

24. X. W. Li, H. X. Dai, J. G. Deng, Y. X. Liu, Z. X. Zhao, Y. Wang, H. G. Yang and C. T. Au, *Appl. Catal. A-Gen.*, 2013, **458**, 11-20.

25. N. A. Merino, B. P. Barbero, P. Grange and L. Cadús, *J. Catal.*, 2005, **231**, 232-244.

26. Z. X. Zhu, Y. N. Shi, C. Aruta and N. Yang, *ACS Appl. Energ. Mater.*, 2018, **1**, 5308-5317.

27. L. Daheron, R. Dedryvere, H. Martinez, M. Menetrier, C. Denage, C. Delmas and D. Gonbeau, *Chem. Mater.*, 2008, **20**, 583-590.

28. V. Bellière, G. Joorst, O. Stephan, F. D. Groot and B. M. Weckhuysen, *J. Phys. Chem. B*, 2006, **110**, 9984-9990.

29. L. Guan, K. Suenaga, S. Okubo, T. Okazaki and S. Lijima, *J. Am. Chem. Soc.*, 2008, **130**, 2162-2163.

30. Z. P. Li, M. Toshiyuki, G. J. Auchterlonie, J. Zou and D. John, *ACS Appl. Mater. Interf.*, 2011, **3**, 2772-2778.

31. H. F. Hu, Y. M. Zhu, X. Y. Shi, Q. Li and R. D. Zhong, *Phys. Rev. B*, 2014, **90**, 134518-134518.
32. S. Yamaguchi, Y. Okimoto and Y. Tokura, *Phys. Rev. B*, 1997, **55**, 8666-8669.
33. I. Fita, V. Markovich, A. Wisniewski, D. Mogilyansky, R. Puzniak, P. Iwanowski, L. Meshi, L. Titelman, V. N. Varyukhin and G. Gorodetsky, *J. Appl. Phys.*, 2010, **108**, 063907.
34. A. Gholizadeh, *J. Am. Ceram. Soc.*, 2017, **100**, 859-866.
35. N. A. Merino, B. P. Barbero, P. Eloy and L. E. Cadus, *Appl. Surf. Sci.*, 2006, **253**, 1489-1493.
36. H. Y. Zhu, P. F. Zhang and S. Dai, *ACS Catal.*, 2015, **5**, 6370-6385.
37. S. M. Zhou, L. Shi, J. Y. Zhao, L. F. He, H. P. Yang and S. M. Zhang, *Phys. Rev. B*, 2007, **76**, 172407.